Optical-gradient-force–induced nonlinearity in coupled microcavities

Xu Guo,[1,*] Jianming Mai,[2,*,†] Haihua Fan,[1] and Kok Wai Cheah[2,‡]

[1]*Guangdong Provincial Key Laboratory of Nanophotonic Functional Materials and Devices, School of Information and Optoelectronic Science and Engineering, Guangdong Basic Research Center of Excellence for Structure and Fundamental Interactions of Matter, South China Normal University, Guang-Zhou 510006, China*

[2]*Department of Physics, Hong Kong Baptist University, Kowloon Tong, Hong Kong SAR 510006, China*

(Received 27 March 2024; accepted 20 June 2024; published 15 July 2024)

The nanosuspension is a stable solid-liquid hybrid fluid formed by suspending solid nanoparticles in a liquid. Based on nanosuspension, an optical-gradient-force–induced optical nonlinear characteristics in a coupled microcavities is theoretically investigated. Under high incident power, the nanoparticles that are in one of the cavities redistribute themselves leading to a significant change of the effective refractive index. The consequence of the redistribution is investigated by solving the nonlinear coupled mode theory equations. Both nonreciprocal transmission and bistability are observed due to disparate forward and backward incident field intensities in the coupled microcavities. Furthermore, the numerical simulation shows details of the mode interaction within the coupled microcavities, and agrees well with the theoretical modeling. This work demonstrates the viability of nanoparticle-mediated nonlinearity in microscale optical systems. The findings open more possibilities for light manipulation in sophisticated microfluidic systems and beyond.

DOI: 10.1103/PhysRevA.110.013509

I. INTRODUCTION

Nonlinearity is a higher-order property of optics and photonics. Nonetheless, it enables many rich phenomena that transcend the limitations of linear optics. Nonlinear optical materials, characterized by their higher-order dependence on electromagnetic field intensities, have not only revolutionized the generation of high-efficiency lasers [1] but have also become instrumental in breaking reciprocity [2–4]. There are many ways to break nonreciprocity, such as magnetooptical material systems [5] and optomechanically coupled systems [6–8]. In contrast, nonlinear materials exhibit well compatibility in different optical platforms, thereby serving as a versatile tool for inducing nonreciprocal behaviors. For example, chip-based LiDAR [9], dielectric metasurfaces [10–12], photonic-crystal [13–15], and ring resonators [16–20].

To explore optical nonreciprocity and bistability, the optical characteristics of multilayer heterostructure with the Kerr effect [21] have been studied. In another work, nonreciprocal transmission is demonstrated in a liquid metamaterial induced by optical gradient force nonlinearity [22]. In this work, the characteristics of optical gradient force nonlinearity in coupled cavities are being investigated.

In this work, a metal-insulator-metal (MIM) slab structure imbued with dynamic nanosuspension is introduced. The nanosuspension is a stable solid-liquid hybrid fluid formed by suspending solid nanoparticles in a liquid [23]. This system exhibits a unique responsiveness where, under the influence of intense incident light, the spatial distribution of the nanosuspension goes through significant redistribution. This modulation directly translates into variation in the effective refractive index of the structure. In particular, the nonuniform field distributions induced by forward and backward incident light result in directionally dependent effective refractive index. This asymmetry is the cause of the nonreciprocal transmission observed in the MIM. This work provides an in-depth theoretical understanding of the optical nonlinearity in the MIM structure, and potentially broadens applications of future nonlinear optical devices.

II. THEORY

As shown in Fig. 1(a) the MIM system consists of twin circular microcavities etched in a metal film, flanked by two air waveguides. The nanosuspension is in cavity A with resonant frequency ω_a, while cavity B with resonant frequency ω_b contains solely the carrier liquid. The light with a frequency of ω incident from left is defined as forward incident, while the light incident from right is defined as backward incident. The subscripts f and b represent forward and backward incident direction, respectively. The coupling strength κ is related to the distance d between two cavities, and the decay rates of the two cavities are Y_a and Y_b, which is related to the intrinsic loss of the material, and to the coupling to the waveguide.

Nonreciprocity is rooted in the optical nonlinearity of nanosuspension. Nonlinearity arises from particle redistribution within the nanosuspension under an electromagnetic field [Fig. 1(b)]. The inhomogeneity of the electric field leads to the local aggregation of particles, which results in a localized increase in the refractive index [Fig. 1(c)]. Thus, the different field distributions of forward and backward propagating can

*These authors contributed equally to this work.
†Contact author: 20482965@life.hkbu.edu.hk
‡Contact author: kwcheah@associate.hkbu.edu.hk

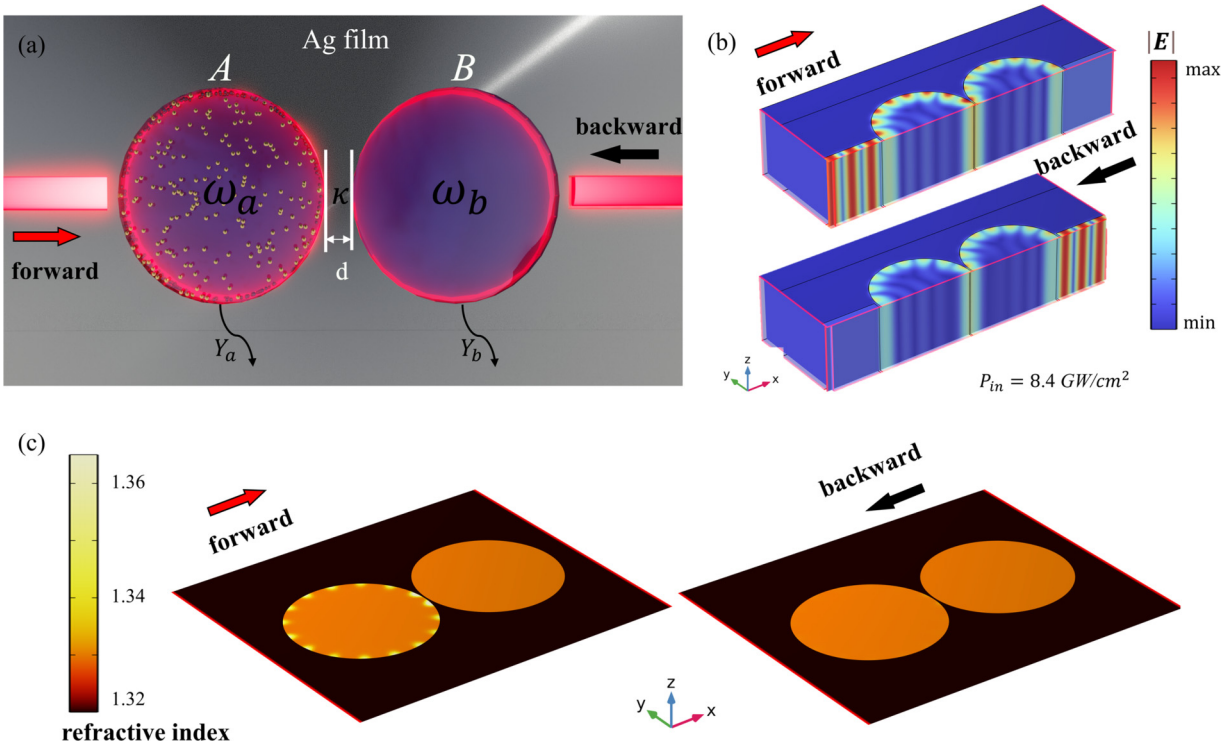

FIG. 1. (a) The MIM resonator structure. The excitation from the left waveguide is defined as forward incident, whereas excitation from the right waveguide is defined as backward incident. (b) Electric field intensity distribution at forward incidence and backward incidence under nonlinear effects (the incident power $P_{\text{in}} = 8.4$ GW/cm^2. (c) The refractive index distribution in the resonator under forward incidence and back incidence when nonlinear effects occur.

lead to the breakdown of reciprocity. In general, in the absence of an external field and in thermal equilibrium, the distribution of particles is randomly distributed inside cavity A. However, optical gradient forces generated by external excitation can disturb the equilibrium distribution of particles in nanosuspensions. In order to describe the expression for the nonlinear effect caused by the optical gradient force, the Nernst-Planck equation is invoked, the particle flux density $\boldsymbol{J}_P$ is given by the Nernst-Planck equation [24]:

$$\boldsymbol{J}_P = \rho_p \mathbf{v} - D\nabla\rho_p, \tag{1}$$

where ρ_p is the particle number density, D is the particle diffusion coefficient, where $\boldsymbol{v} = \mu \boldsymbol{F}$ is the particle drift velocity, which is related to the gradient force $\boldsymbol{F}$, with $\mu = \frac{1}{(6\pi r\eta)}$ represents the particles mobility, in which r is the particle radius, and η is the viscosity of the liquid. When the size of the particles is much smaller than the wavelength of the incident light ($r \ll \lambda$), the electric field inside and near the particles exhibits the characteristics of a static electric field, and the particles are polarized into a synchronously oscillating electric dipole. Through the dipole approximation, the gradient force of light on particles [24,25], $\boldsymbol{F}$, can be derived as:

$$\boldsymbol{F} = \frac{\alpha}{4}\nabla|E|^2, \tag{2}$$

where E is the electric field strength, α the polarizability, which is a function of refractive index n_p of the particles in the suspension, and n_b the background refractive index. The refractive index n_0 of the suspension is affected by n_p and n_b. Defining the refractive index ratio, $m = \frac{n_p}{n_b}$, then the polarizability, can be expressed as:

$$\alpha = 3V_p\varepsilon_0 n_b^2(m^2 - 1)/(m^2 + 2), \tag{3}$$

where V_p is the volume of a single particle, and ε_0 is the vacuum permittivity.

If the concentration of the nanosuspension is low, all interactions between particles can be ignored, and the calculation of the concentration of the suspension is in the Appendix A. Under this condition and in equilibrium stable conditions, it satisfies $\boldsymbol{J}_P = 0$, $\frac{\partial}{\partial t} = 0$, and from Stokes-Einstein relationship, $\frac{\mu}{D} = \frac{1}{k_B T}$, then:

$$\nabla\rho_p = \frac{\alpha\rho_p}{4k_B T}\nabla|E|^2, \tag{4}$$

in which k_B is the Boltzmann constant and T is the temperature in K. The particle number density of the uniform distribution is set as ρ_0, then ρ_p is

$$\rho_p = \rho_0 \exp\left(\frac{\alpha|E|^2}{4k_B T}\right). \tag{5}$$

Consider that the refractive index ratio m is close to 1, the Maxwell-Garnett model can be used to derive that the effective refractive index distribution in the nanosuspension [23]:

$$n_{\text{eff}} = (1 - f_p)n_b + f_P n_p = n_b + f_p(n_P - n_b), \tag{6}$$

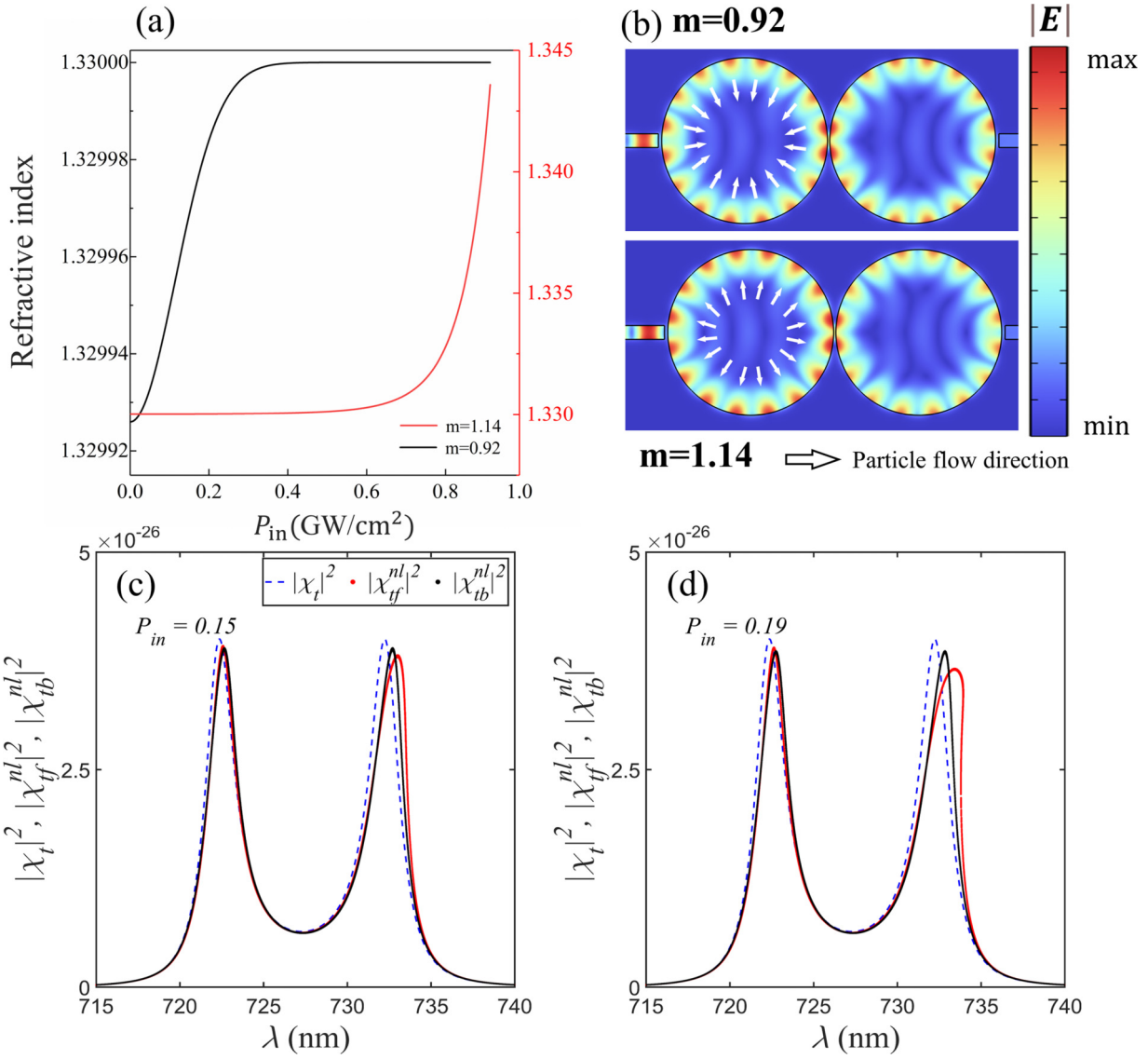

FIG. 2. (a) Incident power as function of local refractive index, the red line indicates $m > 1$ and the blue line indicates $m > 1$. (b) Electric field distribution of $m > 1$ and $m < 1$ suspension microcavities under nonlinear conditions, particle flow direction is indicated by white arrows. The spectrum of $|\chi_t|^2$, $|\chi_{tf}^{\text{nl}}|^2$ and $|\chi_{tb}^{\text{nl}}|^2$ as function of incident wavelength with $\gamma_a = \gamma_b = 2.5 \times 10^{12} - 9 \times 10^{13} i$ rad/s, $\kappa = 1.2 \times 10^{13}$ rad/s, $\lambda_0 = 723$ nm, $d_0 = 340$, $P_{\text{in}} = 0.15$ (c) and $P_{\text{in}} = 0.19$ (d) The blue dashed line is the $|\chi_t|^2$, the red line is the $|\chi_{tf}^{\text{nl}}|^2$, and the black line is the $|\chi_{tb}^{\text{nl}}|^2$.

in which f_p is the volume filling factor in the nanosuspension. When the particle concentration is low, f_p is expressed as:

$$f_p = V_p \rho_0 \exp\left(\frac{\alpha |E|^2}{4 k_B T}\right). \tag{7}$$

From Eq. (6), when the nanosuspension exhibits a positive polarizability ($m > 1$), the local effective refractive index is proportional to the exponential square of electric field strength [red line in Fig. 2(a)], until the refractive index closes to n_p [26]. When the nanosuspension exhibits a negative polarization rate ($m < 1$), the local effective refractive index is inversely proportional to the exponent of the electric field strength square until the refractive index closes to n_b [Fig. 2(a), blue line]. The particle number density is set to $n = 1.9 \times 10^{14}$ cm^{-3}, the refractive index of the low-power state is almost the same as the background liquid. As shown in Fig. 2(b), particles with $m > 1$ are pushed to the regions with lower electric field strength, reducing the local refractive index. Whereas, particles with $m > 1$ accumulate at the regions with the highest electric field strength, making the local refractive index increase with the power until saturation. Since the suspension is inside the microcavity, and the microcavity has a finite volume (Appendix A, Fig. 6). This means it is difficult to produce particle aggregation by relying on the thrust in the case of $m < 1$. Therefore, the mainly discusses on the nonreciprocal phenomenon is on $m > 1$. Discussion on parameters such as microcavity size is provided in Appendix A.

Nonlinear coupling mode theory (NCMT) is used to elucidate the generation of nonreciprocity [27]. To simplify the analysis, $\omega_a = \omega_b = \omega_0$ is assumed and $\widetilde{a}$ and $\widetilde{b}$ represent the

field amplitudes in the two cavities. In addition, ($|\frac{n_0-n_{\text{eff}}}{n_0}| \leqslant 10^{-4}$) is defined as a linear condition because the change in refractive index is subtle that the nonlinear effect is negligible. In the nonlinear regime, a shift of the resonance frequency is observed due to the changing in effective refractive index of nanosuspension in cavity A. For the heterostructure, the NCMT equation describing the forward and backward incident, respectively, in frequency domain is

$$\begin{pmatrix} \omega - (\omega_a - \gamma_a e^{\frac{|\tilde{a}|^2}{d_0}}) + i\gamma_a & -\kappa \\ -\kappa & \omega - \omega_b + i\gamma_b \end{pmatrix} \begin{pmatrix} \tilde{a} \\ \tilde{b} \end{pmatrix} = \begin{pmatrix} -i\sqrt{\kappa_{ea}} A_{\text{in}} \\ -i\sqrt{\kappa_{eb}} B_{\text{in}} \end{pmatrix}, \tag{8}$$

where $i^2 = -1$, $\kappa_{ea(eb)}$ is the loss rate for the coupling between cavity $A(B)$ and the environment. $A_{\text{in}}(B_{\text{in}})$ is the incident light field for forward and backward incident; $\gamma_{a(b)} = Ya(b)/2$ and $\exp(\frac{|\tilde{a}|^2}{d_0})$ is the nonlinear term, where d_0 is the nonlinear factor. For forward incident, $B_{\text{in}} = 0$, and for backward incident, $A_{in} = 0$.

Then the effective susceptibility χ_t^{nl} in the nonlinear regime can be derived as:

$$\chi_t^{\text{nl}} = \frac{-\kappa}{\left[\omega - \left(\omega_a - \gamma_a e^{\frac{|\tilde{a}|^2}{d_0}}\right) + i\gamma_a\right](\omega - \omega_b + i\gamma_b) - \kappa^2}. \tag{9}$$

From Ref. [21], $|t| = |\frac{B_{\text{out}}}{A_{\text{in}}}| = |\sqrt{\kappa_{eb}\kappa_{ea}}\chi_t^{\text{nl}}|$, the transmittance $T = |t|^2 \propto |\chi_t^{\text{nl}}|^2$ for forward $|\chi_{tf}^{\text{nl}}|^2$ and backward $|\chi_{tb}^{\text{nl}}|^2$ incident. Due to the asymmetric $\widetilde{a}$ of the opposite incident, χ_{tf}^{nl} and χ_{tb}^{nl} is not identical.

To elucidate the nonlinear transmittance behavior of the proposed structure, we calculate $|\chi_t|^2$, $|\chi_{tf}^{\text{nl}}|^2$, and $|\chi_{tb}^{\text{nl}}|^2$ under different P_{in}. In Figs. 2(c) and 2(d) there are two resonance peaks for $|\chi_t|^2$ in linear regime (blue dashed line). The longer wavelength peak is designated as peak I, whereas the shorter wavelength peak is designated as peak II. The weak coupling condition with low coupling coefficient κ and only one peak is described in the Appendix B Fig. 8. Whereas, in nonlinear case, peak I and II of $|\chi_{tf}^{\text{nl}}|^2$ (red solid line) and $|\chi_{tb}^{\text{nl}}|^2$ (black solid line) have red-shift bending relative to the linear case. The bending of peak I for $|\chi_{tf}^{\text{nl}}|^2$ is more obvious than that of peak I for $|\chi_{tb}^{\text{nl}}|^2$. The difference in bending between the two directions becomes more significant with the increasing of P_{in} from 0.15 [Fig. 2(c)] to 0.19 [Fig. 2(d)]. Furthermore, the bending degree of peak II for $|\chi_{tb}^{\text{nl}}|^2$ is slightly larger than that for $|\chi_{tf}^{\text{nl}}|^2$.

In Figs. 3 and 9 (Appendix B), $|\chi_{tf}^{\text{nl}}|^2$ (red solid line) and $|\chi_{tb}^{\text{nl}}|^2$ (black solid line) as a function of P_{in} at $\lambda = 734.2$ nm is shown. Distinct optical bistable loops are characterized by three segments: lower, middle, and upper branch. As the incident power P_{in} increases and reaches the terminus of the lower branches, which is defined as the switch-on threshold, there is a sharp switch to the upper branch, indicated by orange arrows. Whereas, as P_{in} decreases to the terminus of upper branches, designated as switch-off thresholds, there is a dramatic drop to the lower branch, indicated by blue arrows. Within this bistability region, even minor perturbations can induce a transition to the more stable upper or lower branches. The difference between the switch-on and switch-off thresholds defines the bistable width. Furthermore, the bistable width of $|\chi_{tf}^{\text{nl}}|^2$ is found to be narrower than that of $|\chi_{tb}^{\text{nl}}|^2$.

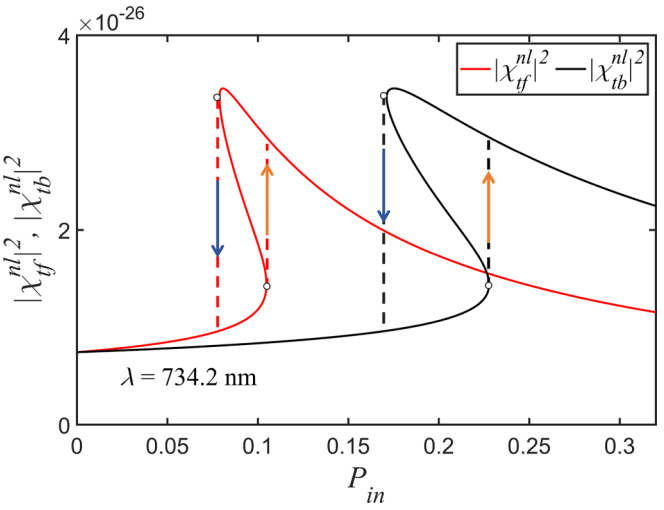

FIG. 3. Optical bistability of the microcavity structure. The orange and blue arrows highlight the switch-on and switch-off behaviors at the optical bistability thresholds, respectively. The red line represents forward incident, and the black line represents backward incident.

III. NUMERICAL SIMULATION RESULTS AND DISCUSSION

COMSOL MULTIPHYSICS is used to simulate the relationship between wavelength and transmittance for both incident directions, the details of the model are shown in Appendix A. Here, two-dimensional (2D) models are used instead of 3D models, which can simplify calculations. When the height of a structure exceeds the skin depth of surface plasmon polaritons (SPPs), which is the case in real photonic devices, the impact of structure height on the losses in the 3D model can be approximated using a 2D model. The material losses exhibit minimal variation when the height of the waveguide exceeds 200 nm. This observation indicates that the waveguide's height no longer significantly impacts material losses. Remarkably, even as the waveguide's height approaches infinity, material losses remain constant—a scenario akin to a 2D simulation [28]. In the system, the radii of cavities A and B are 750 nm, and the widths of waveguides are 125 nm. The coupling characteristic can be tuned by adjusting the gap d, between the double cavities [29]. To maintain strong coupling, the distance d between the two cavities is set at 20 nm. The refractive index of the silver film is obtained from Ref. [30]. Refractive index of the cavities $n_p = 1.52$, $n_b = 1.33$. Furthermore, to validate the universality of the conclusion, an alternative method of waveguide indirect coupling has also been included in the Appendix C (Fig. 10). From the NCMT, strong coupling between twin cavities leads to a significant mode splitting in wavelength domain. As shown in Fig. 4, two

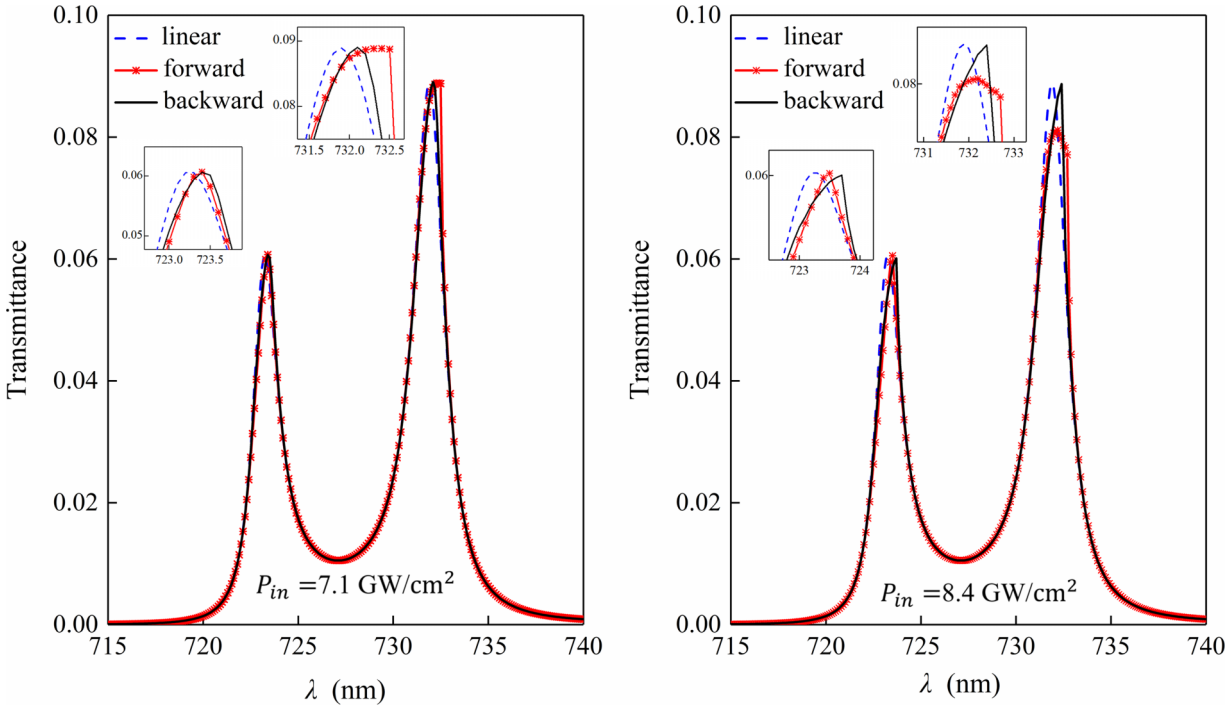

FIG. 4. Transmittance for linear case (blue dashed line), forward incident (red asterisk) and backward incident (black line), when the incident power equals to (a) 7.1 GW/cm^2 and (b) 8.4 GW/cm^2. The radii of cavities A and B are 750 nm, and the widths of waveguides are 125 nm. To maintain strong coupling, d is 20 nm.

splitting transmittance peaks appear at 723.3 nm and 731.9 nm in linear regime, denoted by blue dashed line. Under nonlinear regime, when P_{in} increases to 8.4 GW/cm^2 [Fig. 4(a)], two transmittance peaks show bending toward longer wavelength. Moreover, the two peaks exhibit disparate sensitivities to variations in P_{in}. Compared to the backward incident (black line), the bending in peak I is more significant for the forward incident (red asterisk), attributable to the sequence of light interacting with the nonlinear cavities. This also supports that nonlinearity breaks the reciprocity and leads to an irreversible transmission process. As P_{in} further increasing to 8.4 GW/cm^2 [Fig. 4(b)], the bending of the transmittance peaks become more prominent. Peak I demonstrates that the power increment enhances the nonreciprocal transmission brought about by the nanosuspension.

To further elucidate the characteristics of optical bistability in the system, transmittance for forward and backward incident under varying P_{in} at $\lambda = 732.8$ nm is studied, as shown in Fig. 5(a). To compute the two stable branches of Fig. 3, each simulation step of the incident power is calculated from the previous step value obtained. In Fig. 5(a), the optical bistable loops including increasing (decreasing) step for forward [blue triangle (red asterisk)] and backward [green rhombus (black circle)] incident are observed. When P_{in} gradually increases to about 8.48 GW/cm^2 and 11.1 GW/cm^2 (switch-on thresholds), the transmittance curves switch from the lower branches to the upper branches. However, when P_{in} decreases from a higher value to a lower value, the transmittance curves do not drop until P_{in} reaches 6.93 GW/cm^2 and 9.33 GW/cm^2 (switch-off thresholds). In fact, the switch-on and switch-off threshold for backward incident locate at higher P_{in} than those for forward incident. In addition, the simulation results in Fig. 5(a) are consistent with the theoretical modeling results discussed in Fig. 3. The optical bistability property is also reflected in the asymmetric response to the Gaussian pulse [31], where assuming the pulse duration τ is longer than the cavity mods rise time, and the nonlinear response caused by the suspension is smaller than the optical period, as shown in Fig. 5(b). Response of the structure to the Gaussian pulse is asymmetric, i.e., there are two thresholds for the increasing and decreasing incident power in the bistability.

IV. CONCLUSION

In conclusion, the optical characteristics of a MIM slab with nanosuspension is studied theoretically. It exhibits distinctive nonlinear optical response under the optical gradient force. This response instigates dynamic modulation of the slab's effective refractive index, with significant implications for light manipulation at the microscale. The nonuniform electric field distribution caused by forward and backward incident results in an incident-direction–dependent refractive index, and this asymmetry is responsible for the observed irreversible transmission characteristic. The nonlinear characteristics of the proposed system are described by NCMT, including the optical bistability caused by optical gradient force. The findings reveal that the switching thresholds for backward incident are than those for forward incident, the modeling borne out by our numerical simulations. Further analysis suggests that the structure would produce nonreciprocal transmission response to a Gaussian pulse incident with a duration greater than the material response period. This work provides the theoretical understanding of optical nonlinearity,

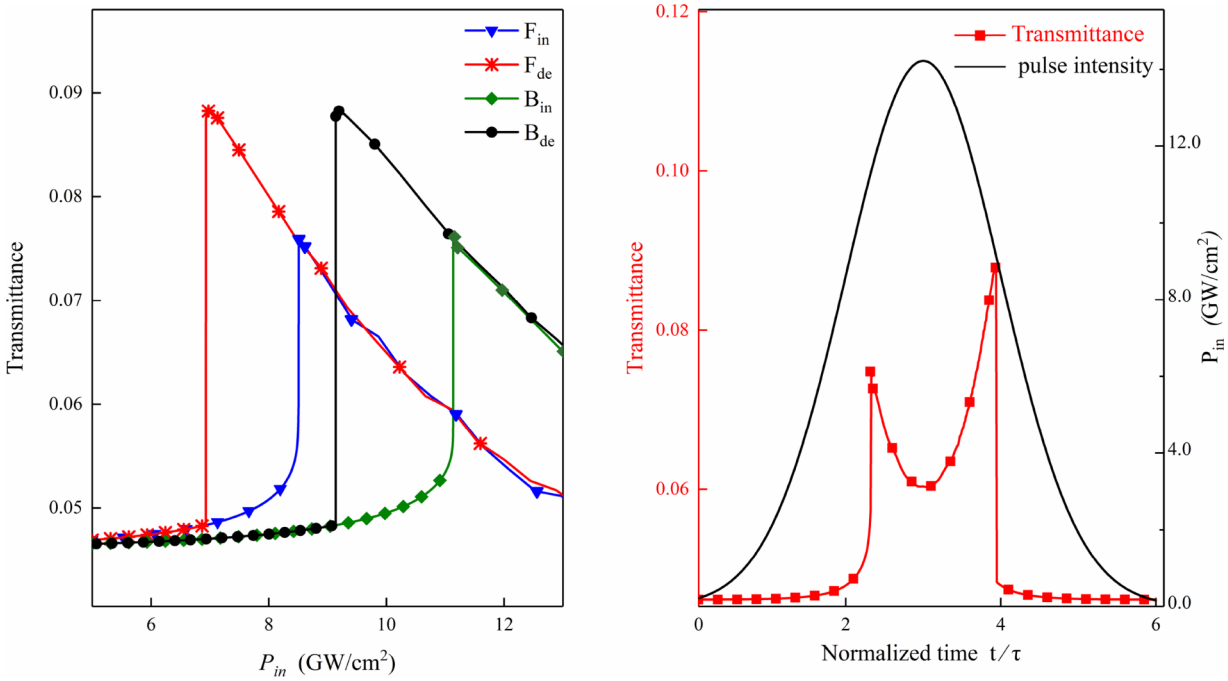

FIG. 5. The optical bistability of the transmittance as a function of P_{in} for forward and backward incident at 732.8 nm. The blue triangle and red asterisk represent the rising and falling branches of forward incidence, respectively. Correspondingly, the green rhombus and black circle represent the rising and falling branches of backward incident, respectively. (b) The asymmetric pulse response predicted by the optical bistability. The transmittance as a function of the normalized time t/τ within a pulse duration. The black line is the input Gaussian time pulse with half-width τ. The red line is the asymmetric response of the transmittance in the presence of bistability

as well as potentially broadening future applications of nonlinear optical devices.

ACKNOWLEDGMENTS

This work was funded by Hong Kong Research Grant Council No. (12303019, AoE/P-02/12).

APPENDIX A: METHODS AND FEASIBILITY OF PARAMETERS

The numerical simulations in the main text use the ELECTROMAGNETIC WAVES FREQUENCY DOMAIN module of COMSOL MULTIPHYSICS. A 2D model as shown in Fig. 1(a) was created, with a rectangular simulation region of dimensions 5 μm × 2.5 μm surrounded by perfectly matched layers. Both circular cavities have a diameter of 1500 nm. The waveguide width on either side of the microcavity is 125 nm, maintaining a distance of 30 nm from the microcavity, and the separation between the two cavities is kept at $d = 20$ nm. Cavity A is designated as a nonlinear cavity with a particle number density of $n = 1.9 \times 10^{14}$ cm^{-3}. The nonlinear behavior of the suspension is obtained from Eq. (6), where $n_b = 1.33$, $n_b = 1.52$, and the particles in the suspension are assumed to be spherical with a diameter of $d_p = 20$ nm. The refractive index of B is set to $n_b = 1.33$. The refractive index of the silver layer is taken from Ref. [30]. Numeric port conditions are set as the light source, and to achieve bistable behavior, different input powers are set in the auxiliary sweep.

In the design of the structure, the size of the cavity directly determines the resonance wavelength and the intensity of the output light, as well as the volume of liquid that can be accommodated, which in turn affects the nonlinearity strength. As shown in Fig. 6, the change of the diameter of two microcavities is calculated by COMSOL, while keeping the distance between the double cavities and the distance between the cavity and the waveguide unchanged. The dependence of the resonance wavelength and the transmittance on the

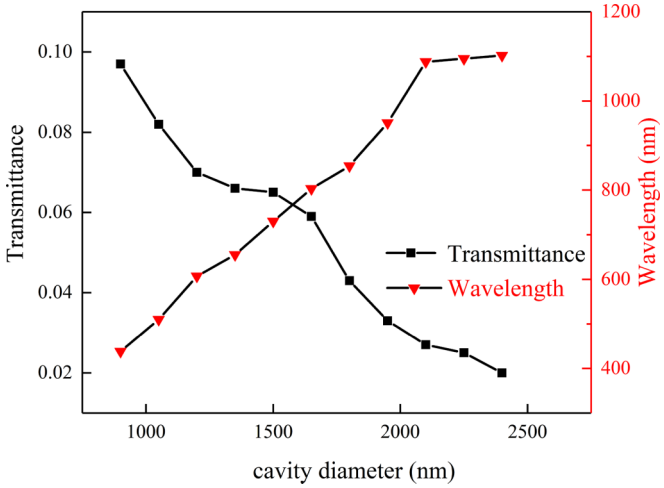

FIG. 6. Resonance wavelengths (red triangle) and transmittances (black square) corresponding to different sizes of double cavities. The widths of waveguides are 125 nm. Distance d between the two cavities is set at 20 nm and refractive index of the cavities $n_p = 1.52$, $n_b = 1.33$.

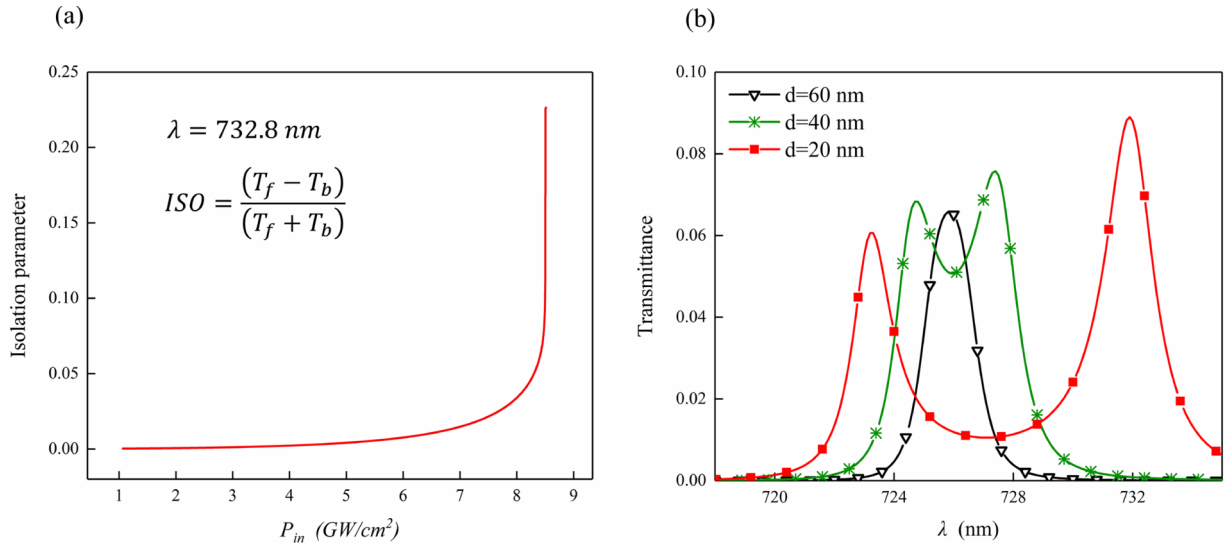

FIG. 7. (a) Forward and backward transmission isolation rates for a two-cavity structure using a microcavity with a diameter of 1500 nm, a particle number density of $n = 1.9 \times 10^{14}$ cm^{-3}, and $d = 20$ nm (using the same parameters as in the main text). (b) Comparison of transmittance when varying only the microcavity spacing d for an incident power of 1×10^{-5} GW/cm^2 (linear condition).

microcavity diameter is obtained. The cavity diameter is positively correlated with the resonance wavelength (red triangle), but negatively correlated with the transmittance (black square).

The choice of the appropriate microcavity size also needs to consider the nonlinearity strength. For the microcavity with a diameter of 1500 nm and the resonance wavelength in red light range, the transmission intensity is not too weak. For particle selection, in the main text, we used polystyrene microspheres with a diameter of $d_p = 20$ nm, forming a particle number density of $n = 1.9 \times 10^{14}$ cm^{-3}. In Eq. (5) of the main text, the exponential law only applies to situations with relatively low concentrations (or filling factors) because the diffusion equation itself neglects the interactions between particles [24]. This requires the size of the microspheres is much smaller than the mean-free path, at room temperature and standard atmospheric pressure, the mean-free path between particles is calculated as [32]:

$$L = \frac{1}{\sqrt{2}\pi {d_p}^2 n} = 2962\ \text{nm}, \tag{A1}$$

which is more than ten times the particle diameter, allowing the interactions between particles to be neglected, meeting the low concentration assumption in Eq. (5). The depth of the cavity is assumed to be 500 nm The percentage of the particle volume in the microcavity is, consistent with the order of magnitude of the filling factor in Ref. [23]. Despite the adoption of the low concentration assumption, the COMSOL model in the main text still exhibits significant nonlinear effects, resulting in noticeable changes in refractive index. This results in nonreciprocity (Fig. 7). The strength of nonreciprocity is represented by the isolation parameter ISO [33], The normalized isolation parameter defined as: $p_{\text{ISO}} = (T_f - T_b)/(T_f + T_b)$.

In addition to the size and particle density of the microcavity, the coupling strength between microcavities should also be discussed. Here, the coupling strength is mainly influenced by the distance d between the microcavities. The smaller the distance, the greater the coupling strength between the cavities. As shown in Fig. 7(a), a microcavity with a diameter of 1500 nm is chosen here, with an incident intensity of 1×10^{-5} GW/cm^2 (under linear conditions). Increasing the coupling strength leads to the splitting of the transmission peak. Specifically, when the mode frequencies of two optical resonant cavities are close, if the coupling strength between them is greater than the system's loss rate, then these two modes will interact, resulting in band splitting [29]. The distance between the two cavities determines the coupling strength. This splitting manifests as two separate peaks in the spectrum, with the size of the splitting determined by the coupling strength—the larger the coupling strength, the more pronounced the splitting. In the main text, we introduced the situation of strong coupling nonreciprocity, where a smaller d under strong coupling results in stronger transmission, while weak coupling requires an increase in d, leading to lower transmission efficiency. However, weak coupling exhibits a more distinct switching power threshold, which we discuss in detail in the next section. The choice of d depends on whether the design requirements lean towards transmission intensity or nonreciprocity.

APPENDIX B: OPTICAL NONRECIPROCITY FOR WEAK COUPLING CONDITIONS

In the double-cavity system, the coupling strength k affects the distribution of the coupling modes, and the weak coupling mode is generated by reducing κ, which is manifested as the increase of the gap d between the double cavities. The weak coupling mode also produces a nonreciprocal phenomenon similar to Fig. 2. As shown in Fig. 8, the two resonance peaks merge when the gap between the double cavities. Unlike the strong coupling case, the weak coupling condition produces a nonreciprocal forward and backward incident power with an

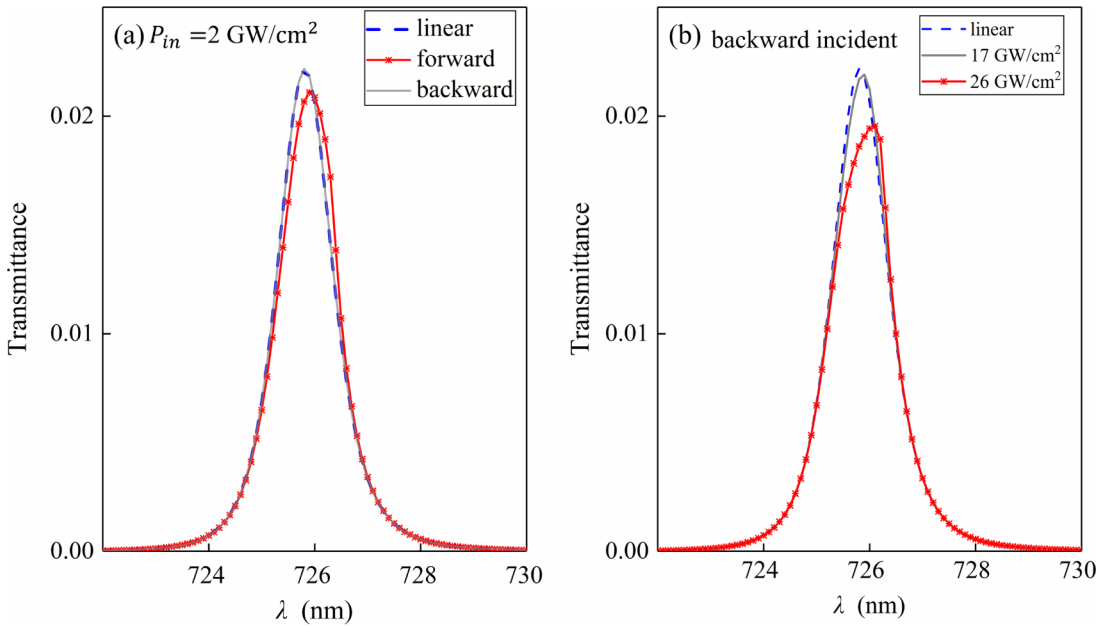

FIG. 8. $d = 80$ nm for the weak coupling condition of transmittance, (a) 2 GW/cm^2 for forward incidence (red asterisk) and backward incidence (light gray line) of the transmittance, and the blue dashed line represents the transmittance for the linear condition. (b) Transmittance for backward incidence condition 17 GW/cm^2 (light gray line) and 26 GW/cm^2, blue dashed line represents the transmittance for the linear condition, and the blue dashed line represents the transmittance for the linear condition.

order of magnitude difference, and only 2 GW/cm^2 can cause the microcavity to have nonlinear effects when the incident is forward, while the incident is almost linear when the incident is backward (Fig. 8). And the backward incident power that produces obvious nonlinear effects requires 26 GW/cm^2, which has a better directional distinction in nonreciprocity, but the increase of the gap between the double cavities also leads to the decrease of the overall transmittance.

Using the NCMT theory to calculate the bistable loop of the weakly coupled mode also verifies the stronger nonreciprocal distinguishability of the weakly coupled mode in the numerical simulation. Without changing other parameters, let $\kappa = 0.2 \times 10^{13}$ rad/s, and Fig. 9 is obtained, where the orange arrow represents the switching threshold of the upper branch of the normal incidence, and the blue arrow represents the switching threshold of the lower branch. The rising threshold (switch-on) and falling threshold (switch-off) of the normal incidence (red line on left side) are one order of magnitude lower than the rising and falling thresholds of the reverse incidence (black line on right side), and the same as the strongly coupled mode is that the bistable loop of the normal incidence is narrower than the bistable loop of the reverse incidence.

APPENDIX C: DIFFERENT WAVEGUIDE COUPLING METHODS

The numerical simulation of the nonreciprocal effect induced by the nanosuspension with other coupling methods further expands the applicability of the theory. As shown in Fig. 10, interconnecting waveguides directly coupled into the microcavity, and indirect evanescent wave coupling can also excite the strong coupling resonance of the dual cavity. Figure 10(a) shows the electric field distribution when the nonlinear effect occurs at the low-energy resonance peak, and the different electric field intensities of the forward and backward incidence result in the nonreciprocity. The nonreciprocity of the structure can be more clearly seen from the transmittance [Fig. 10(b)], and the nonreciprocal behavior of the indirect coupling is similar to that of the waveguide direct coupling, where the nonlinearity is more obvious at the low-energy peak, and the forward incidence is more likely

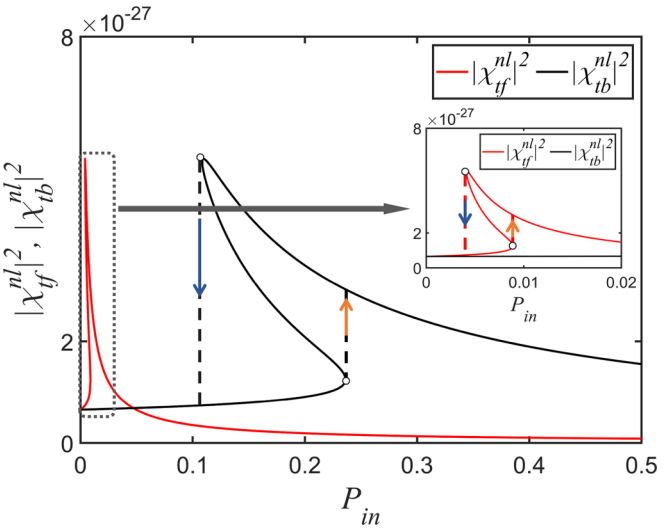

FIG. 9. Optical bistability of weak coupling condition. The orange and blue arrows highlight the switch-on and switch-off behaviors at the optical bistability thresholds, respectively. The red line represents forward incident, and the black line represents backward incident. The inset is an enlarged view of the range of the forward incident bistable loop.

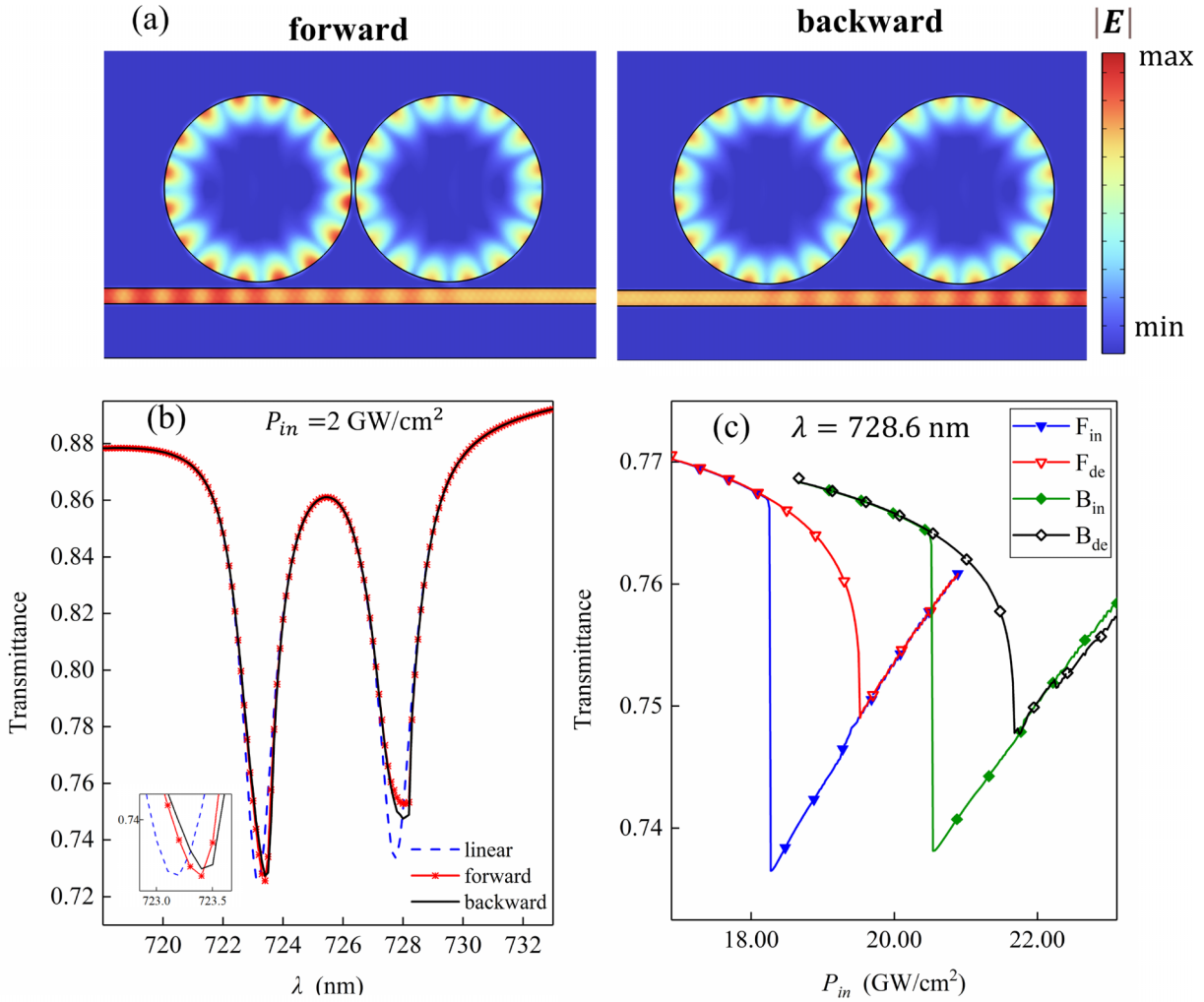

FIG. 10. Interconnecting waveguides directly coupled into the microcavity to form indirect evanescent wave coupling. (a) Electric field distribution at the peak of the low-energy resonance under forward (left) and backward (right) incidence conditions when nonlinear effects occur. (b) Transmittance for linear case (blue dashed line), forward incident (red asterisk line) and backward incident (black line), when the incident power equals to 2 GW/cm^2. (c) The optical bistability of the transmittance as a function of for forward and backward incident. The blue (solid triangle) and red (hollow triangle) lines on left side represent the rising and falling branches of forward incidence, respectively. Correspondingly, the green (solid rhombus) and black (hollow rhombus) lines on right side represent the rising and falling branches of backward incident, respectively.

to reach the nonlinear threshold. The same bistable loop can be obtained [Fig. 10(c)], and the different switching thresholds of the forward and backward incidence are verified. In addition, this evanescent wave coupling method has a higher transmittance, which can ensure the quality of the output light while applying the nonreciprocal phenomenon.

[1] J. Xu, X. Li, J. Xiong, C. Yuan, S. Semin, T. Rasing, and X.-H. Bu, Nonlinear optical perovskites: Halide perovskites for nonlinear optics, Adv. Mater. **32**, 2070017 (2020).

[2] D. Jalas, A. Petrov, M. Eich, W. Freude, S. Fan, Z. Yu, R. Baets, M. Popovi, A. Melloni, J. D. Joannopoulos, M. Vanwolleghem, C. R. Doerr, and H. Renner, What is—and what is not—an optical isolator, Nat. Photon. **7**, 579 (2013).

[3] L. Feng, M. Ayache, J. Huang, Y.-L. Xu, M.-H. Lu, Y.-F. Chen, Y. Fainman, and A. Scherer, Nonreciprocal light propagation in a silicon photonic circuit, Science **333**, 729 (2011).

[4] A. B. Khanikaev and A. Alù, Nonlinear dynamic reciprocity, Nat. Photon. **9**, 359 (2015).

[5] W. Yang, J. Qin, J. Long, W. Yan, Y. Yang, C. Li, E. Li, J. Hu, L. Deng, Q. Du, and L. Bi, A self-biased non-reciprocal magnetic metasurface for bidirectional phase modulation, Nat. Electron. **6**, 225 (2023).

[6] Y. Jiang, S. Maayani, T. Carmon, F. Nori, and H. Jing, Nonreciprocal phonon laser, Phys. Rev. Appl. **10**, 064037 (2018).

[7] Y. Xu, J.-Y. Liu, W. Liu, and Y.-F. Xiao, Nonreciprocal phonon laser in a spinning microwave magnomechanical system, Phys. Rev. A **103**, 053501 (2021).

[8] S. Hua, J. Wen, X. Jiang, Q. Hua, L. Jiang, and M. Xiao, Demonstration of a chip-based optical isolator with parametric amplification, Nat. Commun. **7**, 13657 (2016).
[9] K. Y. Yang, J. Skarda, M. Cotrufo, A. Dutt, G. H. Ahn, M. Sawaby, D. Vercruysse, A. Arbabian, S. Fan, A. Alù, and J. Vukovi, Inverse-designed non-reciprocal pulse router for chip-based lidar, Nat. Photon. **14**, 369 (2020).
[10] D. L. Sounas and A. Alù, Fundamental bounds on the operation of fano nonlinear isolators, Phys. Rev. B **97**, 115431 (2018).
[11] S. S. Kruk, L. Wang, B. Sain, Z. Dong, J. Yang, T. Zent graf, and Y. Kivshar, Asymmetric parametric generation of images with nonlinear dielectric metasurfaces, Nat. Photon. **16**, 561 (2022).
[12] A. Mekawy, D. L. Sounas, and A. Alù, Free-space non reciprocal transmission based on nonlinear coupled fano metasurfaces, Photon. **8**, 139 (2021).
[13] X.-S. Lin, J.-H. Yan, L.-J. Wu, and S. Lan, High trans mission contrast for single resonator based all-optical diodes with pump-assisting, Opt. Express **16**, 20949 (2008).
[14] Y. Yu, Y. Chen, H. Hu, W. Xue, K. Yvind, and J. Mork, Nonreciprocal transmission in a nonlinear photonic crystal fano structure with broken symmetry: Nonrecip rocal transmission in a nonlinear fano structure, Laser Photon. Rev. **9**, 241 (2015).
[15] C. Li, S.-Y. Wu, and J.-F. Wu, Broad-band, re versible nonreciprocal light transmission based on a single nanocavity, Opt. Express **27**, 16530 (2019).
[16] L. Chang, X. Jiang, S. Hua, C. Yang, J. Wen, L. Jiang, G. Li, G. Wang, and M. Xiao, Paritytime symmetry and variable optical isolation in activepassive-coupled mi croresonators, Nat. Photon. **8**, 524 (2014).
[17] B. He, L. Yang, X. Jiang, and M. Xiao, Transmission nonreciprocity in a mutually coupled circulating struc ture, Phys. Rev. Lett. **120**, 203904 (2018).
[18] T. Li, Z. Gao, and K. Xia, Nonlinear-dissipation-induced nonreciprocal exceptional points, Opt. Express **29**, 17613 (2021).
[19] A. D. White, G. H. Ahn, K. V. Gasse, K. Y. Yang, L. Chang, J. E. Bowers, and J. Vučković, Integrated passive nonlinear optical isolators, Nat. Photon. **17**, 143 (2022).
[20] L. Del Bino, J. M. Silver, M. T. M. Woodley, S. L. Steb bings, X. Zhao, and P. Del'Haye, Microresonator isola tors and circulators based on the intrinsic nonreciprocity of the kerr effect, Optica **5**, 279 (2018).
[21] J. Mai and K. W. Cheah, Nonreciprocal transmission in a nonlinear coupled heterostructure, Opt. Express **30**, 46357 (2022).
[22] A. Zharov, V. Fierro, and A. Celzard, Non-reciprocal electromagnetic metasurface based on the nonlinearity of a liquid metamaterial, Opt. Lett. **48**, 5033 (2023).
[23] X. Liang, Z. Zhang, D. Li, X. Han, F. Gao, and Z. Chen, Curved volume waveguides induced by airy beams in neg ative polarizability nanosuspensions, Opt. Commun. **437**, 90 (2019).
[24] R. El-Ganainy, D. N. Christodoulides, C. Rotschild, and M. Segev, Soliton dynamics and self-induced transparency in nonlinear nanosuspensions, Opt. Express **15**, 10207 (2007).
[25] A. Ashkin, J. M. Dziedzic, J. E. Bjorkholm, and S. Chu, Observation of a single-beam gradient force optical trap for dielectric particles, Opt. Lett. **11**, 288 (1986).
[26] M. Matuszewski, W. Krolikowski, and Y. S. Kivshar, Spatial solitons and light-induced instabilities in colloidal media, Opt. Express **16**, 1371 (2008).
[27] V. Grigoriev and F. Biancalana, Nonreciprocal switching thresholds in coupled nonlinear microcavities, Opt. Lett. **36**, 2131 (2011).
[28] H. Shi, S. Yan, X. Yang, X. Wu, W. Wu, and E. Hua, A nanosensor based on a metal-insulator-metal bus waveguide with a stub coupled with a racetrack ring resonator, Micromachines **12**, 495 (2021).
[29] J. Mai, Y. Chen, G. Li, and K. W. Cheah, Double exceptional points in grating coupled metal-insulator-metal heterostructure, Opt. Express **30**, 40053 (2022).
[30] P. B. Johnson and R. W. Christy, Optical constants of the noble metals, Phys. Rev. B **6**, 4370 (1972).
[31] Z. Huang, A. Baron, S. Larouche, C. Argyropoulos, and D. R. Smith, Optical bistability with film-coupled meta surfaces, Opt. Lett. **40**, 5638 (2015).
[32] Richard S. Conroy, Brian T. Mayers, Dmitri V. Vezenov, Daniel B. Wolfe, Mara G. Prentiss, and George M. Whitesides, Optical waveguiding in suspensions of dielectric particles, Appl. Opt. **44**, 7853 (2005)
[33] B. Jin and C. Argyropoulos, Nonreciprocal transmission in nonlinear pt-symmetric metamaterials using epsilon-near-zero media doped with defects, Adv. Opt. Mater. **7**, 1901083 (2019).